FULL PAPER

Precise Structural Development and its Correlation to Function in Conjugated Polymer: Fullerene Thin Films by Controlled Solvent Annealing

Huipeng Chen, Sheng Hu, Huidong Zang, Bin Hu, and Mark Dadmun*

The impact of controlled solvent vapor exposure on the morphology, structural evolution, and function of solvent-processed poly(3-hexylthiophene):[6,6]-phenyl-C_{61}-butyric acid methyl ester (P3HT:PCBM) bilayers is presented. Grazing incident wide angle X-ray scattering (GIWAXS) shows that the crystallization of P3HT increases with solvent exposure, while neutron reflectivity shows that P3HT simultaneously diffuses into PCBM, indicating that an initial bilayer structure evolves into a bulk heterojunction structure. Small angle neutron scattering (SANS) shows the agglomeration of PCBM and the formation of a PCBM pure phase when solvent annealing for 90 min. The structural evolution can be described as occurring in two stages: the first stage combines the enhanced crystallization of P3HT and diffusion of PCBM into P3HT, while the second stage entails the agglomeration of PCBM and formation of a PCBM pure phase. The phase separation of PCBM from P3HT is not driven by P3HT crystallinity, but is due to the concentration of PCBM exceeding the miscibility limit of PCBM in P3HT. Correlation of the morphology to photovoltaic activity shows that device performance significantly improves with solvent annealing for 90 min, indicating that both sufficient P3HT crystallization and formation of a PCBM pure phase are crucial in the optimization of the morphology of the active layer.

1. Introduction

Conjugated polymers are intriguing materials due to their potential use in organic electronics such as low cost, flexible solar cells, low-voltage field-effect transistors and organic optoelectronic devices such as modulators, optical filters, and polarization rotators. One example is organic photovoltaics (OPV), which have attracted significant interest as materials for sustainable solar energy conversion, due to their low cost, flexibility, ease of processing, and straightforward thin film formation.[1–8] The fabrication of OPV active layers occurs by either forming a donor/acceptor bilayer heterojunction or forming a bulk heterojunction (BHJ) structure from a mixture of a donor and a acceptor. A typical BHJ active layer is obtained by spin casting a solution of conjugated polymer mixed with fullerene, where nanoscale interpenetrating networks are formed upon solvent evaporation. However, as-cast devices often exhibit poor photovoltaic efficiencies, and subsequent processing, such as thermal annealing[9–11] and solvent vapor annealing[4,12–16] are required to improve the photovoltaic efficiency.

Previous studies ascribe the increased efficiency in poly(3-hexylthiophene):[6,6]-phenyl-C_{61}-butyric acid methyl ester (P3HT:PCBM) BHJs with thermal annealing to an increase in P3HT crystallinity,[17] which improves hole transport, as well as the agglomeration of PCBM.[18,19] It is reasoned that the increase in charge carrier mobility with thermal annealing is due to an increase of the in-plane π–π stacking of P3HT, where charges can easily transport from one grain to another.[20–24] Moreover, the agglomeration of PCBM in P3HT:PCBM BHJ materials provides pathways for electron transport, which improves the device efficiency as well.[18] Wu and coauthors captured the growth of PCBM domains with the enhanced crystallization of P3HT within seconds of annealing at 150 °C in P3HT:PCBM BHJs.[19] They conclude that the agglomeration of PCBM and enhanced crystallization both contribute to the structure development and increase of device efficiency.

The first bilayer heterojunction solar cell was introduced by Tang in 1986,[25] which is fabricated by consecutively depositing donor and acceptor layers separately and can be broadly applied to layer to layer lamination and roll to roll processes. However, the bilayer structure requires thin layers to allow for exciton transport to and dissociation at the biphasic interface. This minimizes photon absorption, resulting in low 1% power conversion efficiencies (PCE).[25] Sun and Heeger have compared the

Dr. H. P. Chen, Prof. M. Dadmun
Department of Chemistry
University of Tennessee
Knoxville, TN 37996, USA
E-mail: Dad@utk.edu

S. Hu
Department of Chemical and Biomolecular Engineering
University of Tennessee
Knoxville, TN 37996, USA

H. D. Zang, Prof. B. Hu
Department of Material Science and Engineering
University of Tennessee
Knoxville, TN 37996, USA

Prof. M. Dadmun
Chemical Science Division
Oak Ridge National Lab, Oak Ridge, TN 37831, USA

ADVANCED
FUNCTIONAL
MATERIALS
www.afm-journal.de

Materials
Views
www.MaterialsViews.com

function of a bilayer heterojuction which was formed by spinning coating PCBM on the top of P3HT and a bulk heterojunction of P3HT:PCBM which is fabricated by spin-coating the active layer from a mixture of 1:0.8 P3HT:PCBM. In this report, they show no significant difference in structure after thermal annealing the two active layers, and similar PCEs.[26] These results make sense in light of recent results that show that PCBM is considerably miscible in P3HT, where the interdiffusion of PCBM and P3HT occurs with thermal annealing.[26–38] In fact, the rapid diffusion of PCBM into P3HT with thermal annealing in P3HT:PCBM bilayers has been reported by several groups.[26,29–31] Lee and coauthors have also studied solution processed P3HT:PCBM bilayers fabricated by spinning coating PCBM on the top of a spin coated P3HT layer. These results show that a significant amount of PCBM diffuses into P3HT during processing and after thermal annealing, and provides similar PCBM depth profiles and PCE as a P3HT:PCBM BHJ.[31]

Unfortunately, using thermal annealing (TA) to modify the morphology of a BHJ has limitations, in that large scale phase separation and the formation of structures that could be detrimental to the solar-cell performance have been reported.[39] For instance, extended thermal annealing has been shown to create large PCBM crystals, from a few micrometers in size up to 100 μm.[40] Thermal annealing might also degrade the conjugated polymers. Moreover, because the structure develops very quickly with thermal annealing, detailed information on the processes that control the structural development are difficult to experimentally monitor with thermal annealing. For instance, Wu and coauthors studied P3HT:PCBM BHJ thin films during thermal annealing by synchrotron grazing-incident X-ray scattering and their results show the growth of PCBM domains accompanied by the enhanced crystallization of P3HT within seconds of annealing at 150 °C.[19] Because of the rapid structural changes, crystallization and phase separation cannot be examined separately.[19] Because of this swift structural development, it is not clear whether the P3HT crystallization drives the phase separation or the crystallization and phase separation are independent processes.

On the other hand, solvent annealing (SA) provides more precise morphological control.[41] SA is a versatile method where a thin film is exposed to an atmosphere of solvent vapors that diffuse into the deposited layer, the extent of which is dependent on and thus controllable by exposure time. The solvent increases molecular mobility of the components in the active layer, allowing the system to evolve towards a more thermodynamically stable morphology.[42,43] However, there have been few studies that carefully monitor the development of the morphology of BHJ active layers during solvent annealing and correlate these changes to its OPV function changes.[41] Moreover, there are no reports that monitor the changes in morphology and OPV function that occur in an initial conjugated polymer:fullerene bilayer with solvent annealing. Given the promise of bilayer heterojunctions and solvent annealing, a more thorough understanding of the morphological development in these materials using solvent annealing and its correlation to OPV function is needed.

In the present work, the changes in morphology, crystallinity, and depth profile of solvent processed P3HT:PCBM "bilayer" films are monitored using grazing incidence wide-angle X-ray scattering (GIWAXS), neutron reflectivity (NR), and small angle neutron scattering (SANS). Neutron scattering is a very effective technique to characterize the structure and depth profiles of P3HT:PCBM thin films due to the significant scattering length density contrast between P3HT and PCBM. Novel information that separately documents the enhanced crystallization of P3HT, the agglomeration of PCBM, and the inter-diffusion of P3HT and PCBM as a function of controlled solvent vapor exposure is provided with these experimental techniques and are compared to similar changes that occur via thermal annealing. The structural changes are also correlated to the photovoltaic activity of the active layer to provide guidelines by which the active layer of conjugated polymer/fullerene heterojunctions may be optimized with controlled solvent exposure.

More generally, the results provide insight into the relationship between changes in P3HT crystallinity and phase separation between P3HT and PCBM. The PCBM phase separation occurs after the initial increase in P3HT crystallization as well as the diffusion of PCBM into the P3HT. The increase in P3HT crystallization does not, by itself, induce PCBM phase separation. These results clearly show that the phase separation of PCBM from P3HT is associated with the thermodynamic driving force of mixing as it reaches the PCBM miscibility limit in P3HT, and is not driven by the polymer crystallization.

2. Results

2.1. Crystallization of P3HT

The GIWAXS results of the bilayers before and after solvent annealing are presented in **Figure 1**. All of the GIWAXS curves exhibit a peak at $Q \approx 0.39$ Å^{-1}, which corresponds to the P3HT lamellae D$_{100}$ peak. The area under the 100 peak and the sharpness of the peak varies among the samples, which indicates a transformation in crystallinity and crystal size with solvent exposure and thermal annealing. These scattering curves are analyzed to determine the area of the P3HT (100) peak, which is proportional to the crystallinity, and crystal size, using Scherrer's equation[44] (Equation 1).

$$D = \frac{K\lambda}{\beta \cos(\theta)} \qquad (1)$$

In Equation 1, D is the crystal size; K is shape factor, which is assumed to be 0.9 in the present work; λ is the X-ray wavelength; θ is the Bragg angle; and β is the full width at half-maximum of the peak. The (100) peak is fit to a Gaussian with a linear baseline over the same q-range for all samples, an example of which is presented in the Supporting Information. The results of these analyses are shown in **Table 1**, which indicates that the P3HT crystallinity and crystal size increases with solvent exposure time from 0 to 60 min; for instance, the crystallinity increases by 37% with SA of 60 min. Moreover, when the sample is exposed to solvent vapor for an additional 30 min(for a total exposure time of 90 min), the crystallinity remains nearly constant while the crystal size increases from 11.5 nm to 12.6 nm. This is interpreted to indicate that the extended solvent exposure allows the formation of more perfect
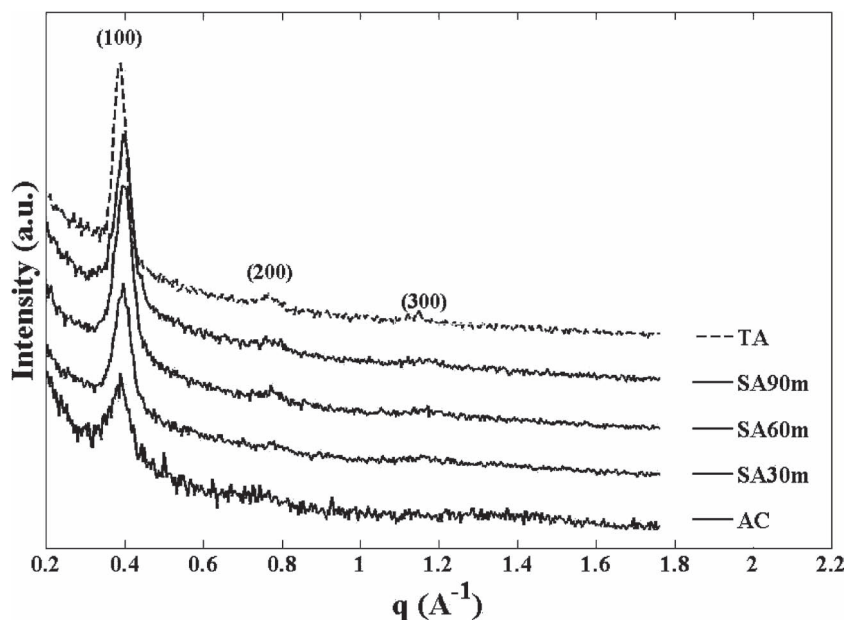
Figure 1. GIWAXS scans of all the samples.

and larger crystals, which may result from the dissolution of smaller crystals by the solvent. As shown in Table 1, the crystallinity and crystal size also increases with thermal annealing, which is consistent with previous reports.[19,30] The similar OPV performance of the SA and TA suggests that the morphology of the samples created by the two protocols have similar structural components, while SA provides more crystallinity and smaller crystals, as shown in Table 1. Moreover, the absence of the diffraction peak at $Q = 1.39$ Å^{-1} that is associated with PCBM crystals indicates that here are no PCBM crystals in all samples.

2.2. Diffusion of PCBM into P3HT with Solvent Annealing

The experimentally determined specular neutron reflectivities, as well as those of the fitted model, are presented in **Figure 2** for the as-cast (AC) and 90 min solvent annealed (SA90m) samples. The data are plotted as RQ^4 as a function of Q to more clearly observe deviations between the experimental and fitted reflectivities. Inspection of Figure 2 shows that the reflectivity of the as-cast bilayer contains oscillations in the Q range between 0.01–0.1 Å^{-1}, which are associated with the bilayer structure of P3HT and PCBM. These oscillations dampen in the reflectivity curve of the solvent annealed sample, indicating a loss of the PCBM layer with solvent annealing, due to the diffusion of the PCBM into the P3HT layer. The scattering length density (SLD)

profiles of the models are then analyzed to extract the depth profile of PCBM in the thin film, which further verifies this interpretation. The PCBM depth profiles of the as-cast and 90 min. solvent annealed samples are presented in **Figure 3**. This analysis shows that the thickness of PCBM in the initial bilayer is about 200 Å with a rough surface. The surface roughness of the PCBM layer is due to the limited thickness of this film. A significant amount of PCBM immediately mixes in the P3HT layer during the fabrication process. Examination of the plateau region of the as-cast thin film at $z \approx 320$–560 Å demonstrates that the PCBM homogeneously mixes with P3HT at a loading of PCBM of $\approx25\%$ during the fabrication process. This is consistent with previous reports that analyzed the depth profile of an as-cast P3HT:PCBM bilayer that is fabricated by the same method.[31] One reason for this interpenetration during processing is that dichloromethane (PCBM solvent) is a marginal solvent for P3HT, which dissolves low mole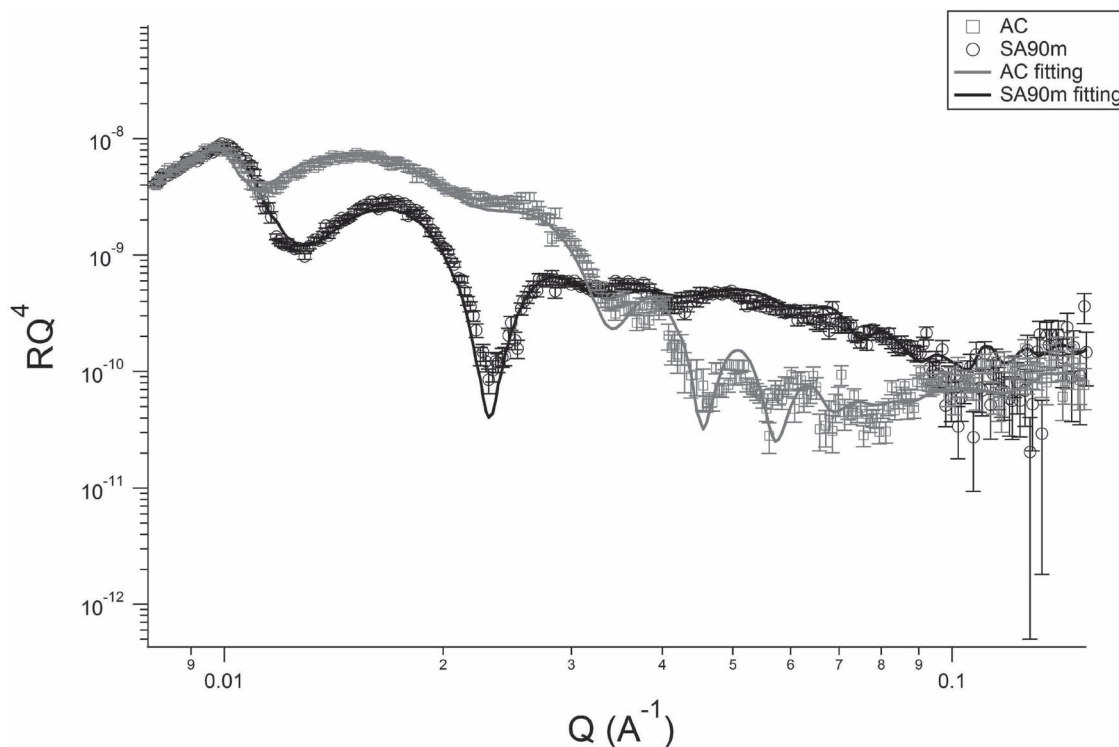cular weight P3HT and swells the interface between the P3HT and PCBM. This interaction results in the diffusion of PCBM into P3HT during the fabrication process. The resultant PCBM depth profile quickly changes with solvent annealing. For the first 30 to 60 min of solvent exposure PCBM diffuses into the P3HT layer, forming a homogeneous mixture of P3HT and PCBM. The plateau region of this sample ($z \approx$ 300–450) contains PCBM at a loading of 34%, and the depth profile is similar to that of a P3HT:PCBM bulk heterojunction mixtures that are thermally annealed.[28,31]

These results imply that a bilayer heterojunction structure evolves into a bulk heterojunction structure with solvent vapor annealing, which is similar to previous reports on thermal annealing of initial bilayers.[29–32] For instance, Lee and coauthors report the diffusion of PCBM into P3HT with thermal annealing of solution-processed bilayers and found there is 35% PCBM homogenously distributed in the P3HT.[31] Additionally, the PCBM selective segregates to the silicon surface in this thin film, which is also consistent with previously reported results with thermal annealing.[31,45]

The similar diffusion of PCBM into P3HT with SA or TA suggests that the depth profiles of the samples created by the two protocols are comparable. Neutron reflectivity, however, only provides information on the depth profiles of PCBM in these samples, but does not provide information on the evolution of the in-plane structure of the sample with solvent annealing. To garner that information, including PCBM phase separation, small angle neutron scattering is required.

## 2.3. PCBM Phase Separation and Structural Development with Solvent Annealing

Thus, the SANS curves of all of the samples were obtained and are presented in **Figure 4**. The scattering intensity at

Table 1. Area of P3HT (100) peak and P3HT crystal size for all the samples.

	AC	SA30m	SA60m	SA90m	TA30m
Area	732	758	990	992	855
Crystal size (±2 Å)	103	114	115	126	156

ADVANCED
FUNCTIONAL
MATERIALS

www.afm-journal.de

FULL PAPER

www.MaterialsViews.com

Figure 2. Reflectivity curves of as-cast (AC) and solvent annealed for 90 min (SA90m) samples. The lines are fits to model scattering density profiles.

$q \approx 0.003–0.03$ increases with solvent annealing time and dramatically increases when the sample is exposed to solvent annealing for the final 30 min (SA for a total of 90 min). Figure S2 (Supporting Information) shows the data as Lorentz-corrected scattering (IQ^2 vs Q), which accentuates the correlation peaks at $Q \approx 0.02$ Å. This peak corresponds to the long period of the P3HT lamellae, which is the mean average distance of two adjacent lamellae. The corresponding long period ($2\pi/Q_{max}$) of
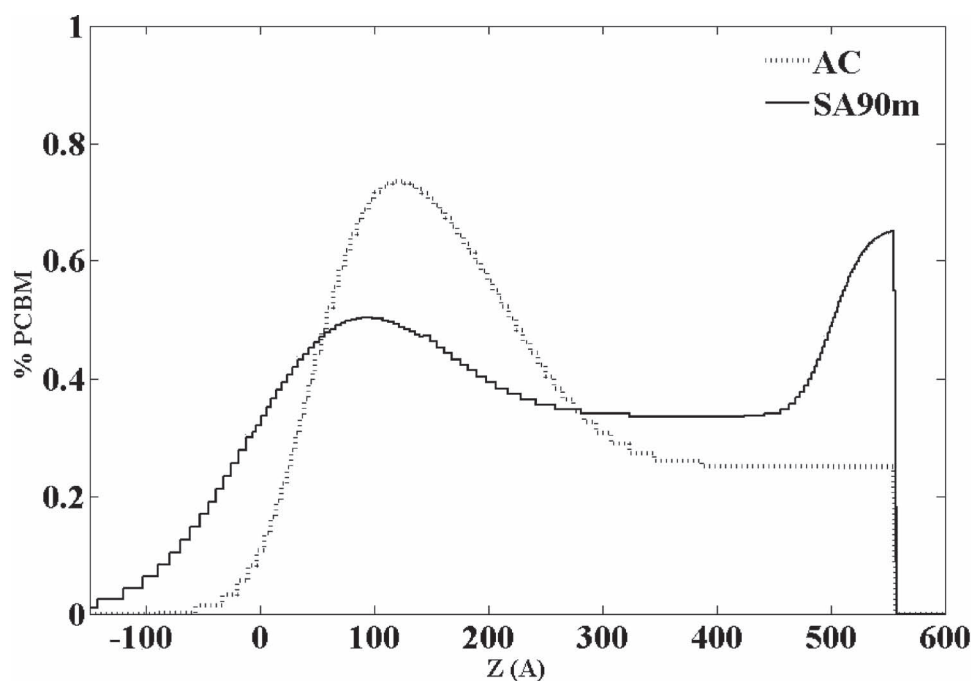
Figure 3. PCBM volume fraction profile in P3HT/PCBM bilayer of as-cast (AC) and solvent annealed for 90 min (SA90m) samples as determined from the reflectivity curves shown in Figure 2.

www.MaterialsViews.com

ADVANCED
FUNCTIONAL
MATERIALS

www.afm-journal.de

FULL PAPER
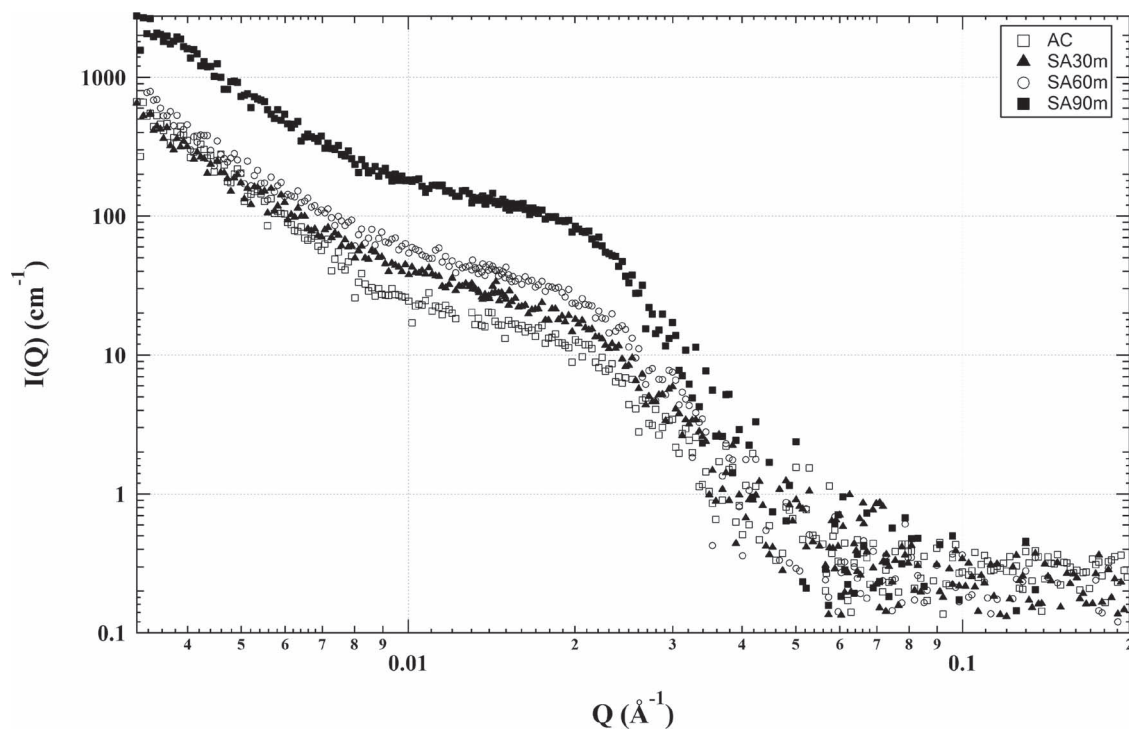
Figure 4. The absolute SANS intensity of as-cast sample and all solvent annealed samples.

these samples are presented in **Table 2**, which shows that the long period of all the samples slightly increases with solvent annealing, which is associated with the thickening of crystalline lamellae, verified by GIWAXS, and is consistent with the diffusion of PCBM into amorphous P3HT, as the reflectivity results reveal.

Moreover, the dramatic increase of scattering after solvent annealing for 90 min can be more clearly observed in Figure S2 (Supporting Information), which indicates a dramatic increase of the SLD contrast (SLDC) between phases. Previous work shows that the scattering intensity of P3HT:PCBM 1:1 thin films dramatically increases with thermal annealing, and is associated with the agglomeration of PCBM and the formation of PCBM domains.[18]

To analyze the scattering patterns and obtain quantitative structural information from the SANS curves, a picture of the phases that exist in the system must be addressed first. The ideal morphology of P3HT:PCBM BHJ active layers has often been described as a bicontinuous system that comprises pure phased separated donor and acceptor domains. However, recent results clearly show that P3HT and PCBM are considerably miscible,[27,28,32,45] which means that the BHJ active layer consists of three phases; a P3HT crystalline phase, a PCBM rich

Table 2. P3HT crystal long period calculated from the correlation peaks in Lorentz-corrected scattering pattern.

	AC	SA30 m	SA60 m	SA90 m
Long period (±2 Å)	292	306	314	320

phase, and a miscible phase of amorphous P3HT and PCBM.[32] The miscibility limit of PCBM in P3HT has recently been reported to be 22%.[45]

However, the structure of an as-cast spin-coated bulk heterojunction is dominated by the deposition process, resulting in the relatively homogeneous distribution of PCBM throughout the sample. Thus, the morphology of the as-cast sample can be approximated as a two-phase system, which consists of P3HT crystals that are distributed in a homogenous mixture of amorphous P3HT and amorphous PCBM.[32] With annealing, the PCBM phase segregates from the amorphous P3HT because its concentration in the amorphous P3HT phase is above the 22% miscibility limit,[45] resulting in the agglomeration of PCBM and the formation of a third phase that is rich in PCBM.

In the neutron scattering of this phase separated structure, the measured scattering intensity is a sum of the scattering between the P3HT crystal and the PCBM phase, between the P3HT crystal and the miscible amorphous phase and between the PCBM phase and the miscible phase. The contribution of each phase pair to the total scattering is proportional to the square of the difference of the scattering length density of the two phases, $(b_i - b_j)^2$. Examination of the scattering length density contrast (SLDC) of these three pairs, clearly shows that the contrast between the P3HT crystals (0.69×10^{-6} Å^{-2}) and the P3HT:PCBM miscible phase (1.38×10^{-6} Å^{-2}) is very small relative to the contrast between pure PCBM (4.4×10^{-6} Å^{-2}) and either P3HT containing phase (or a mixture of the two).[40] Moreover, the SLDC between PCBM and P3HT crystals can be approximated to equal the SLDC between PCBM and the miscible PCBM/P3HT phase without significant loss of accuracy in

ADVANCED
FUNCTIONAL
MATERIALS
www.afm-journal.de

www.MaterialsViews.com

FULL PAPER

further analysis. Based on this analysis, the scattering is dominated by the structure of the PCBM phase. Hence, for the following SANS analysis, the three-phase system can be described as the PCBM phase dispersed in a P3HT rich phase.

If the P3HT:PCBM mixture can be analyzed as a two-phase system that consists of a P3HT crystal phase dispersed in an amorphous mixture of P3HT and PCBM, its scattering pattern is accurately modeled as an elliptical cylinder model.[32,46] This is because the elliptical cylinder accurately models the lamellar structure of the P3HT crystals that are dispersed in the amorphous mixture of P3HT and PCBM. Alternatively, the system that contains a phase separated PCBM phase is accurately modeled with a Schultz sphere model,[18,48] which describes a system where spheres (PCBM domain) are dispersed in the matrix (the P3HT rich phase). In these analyses, the size of the scattering structure (elliptical cylinder or sphere) as well as the scattering contrast between the structure and the surrounding matrix can be determined from the fitting of the scattering curve to the model. The use of different models for the system before and after the formation of PCBM pure phase is due to the different shapes of P3HT crystal and PCBM domain, where P3HT crystal is modeled as an elliptical cylinder shape and the PCBM domain is modeled as a sphere.

To verify which structural model fits the as-cast sample and solvent annealed samples, all scattering curves were first fit to the elliptical cylinder model.[32,46] From this analysis, the scattering length density contrast between the P3HT crystal and surrounding matrix (a mixture of amorphous P3HT and PCBM) is obtained. **Figure 5** shows that the scattering curves

Table 3. Cylinder SLD, solvent SLD, and calculated PCBM vol% in surrounding solvent (mixture of amorphous P3HT and PCBM) obtained from the elliptical cylinder model.

	AC	SA30m	SA60m	SA90m
Cylinder SLD ($\times 10^{-6}$ A^{-2})	0.68	0.68	0.68	0.68
Solvent SLD ($\times 10^{-6}$ A^{-2})	1.71	1.92	2.13	2.71
PCBM in amorphous P3HT/PCBM ($\pm 1\%$)	28%	34%	40%	55%

are successfully fit to the elliptical cylinder model, where the structural parameters from these fits are presented in **Table 3**. The volume fraction of PCBM that is dissolved in the amorphous P3HT is obtained from the scattering length density contrast of the fit because the scattering length density of crystalline P3HT is known. The results of this calculation are also shown in Table 3. This analysis shows that the as-cast sample consists of P3HT crystals dispersed in an amorphous matrix that contains 28% PCBM, which is consistent with the neutron reflectivity results that indicate that this sample contains a layer that is 25% PCBM in the P3HT matrix.

As the sample is solvent annealed, the amount of PCBM in the amorphous P3HT matrix increases to 34% at 30 min and 40% at 60 min, indicating that the primary process during the first 60 min of solvent annealing is the intermixing of the two layers, which again agrees with the reflectivity results. It must be emphasized, however that the reflectivity experiments provide a measure of the amount of PCBM fraction in the complete
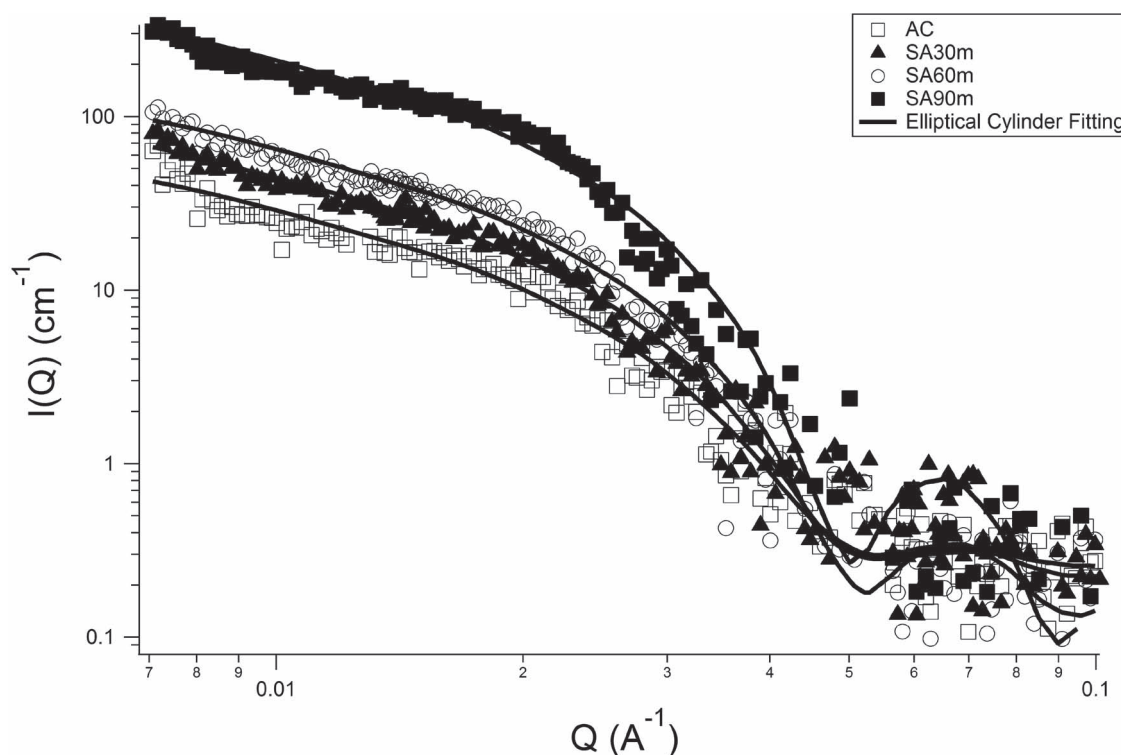
Figure 5. Fit of the structure factor of the as-cast and all solvent annealed samples to the scattering of an elliptical cylinder, which models the lamellar structure of the P3HT crystals. Parameters extracted from these fits are given in Table 3.
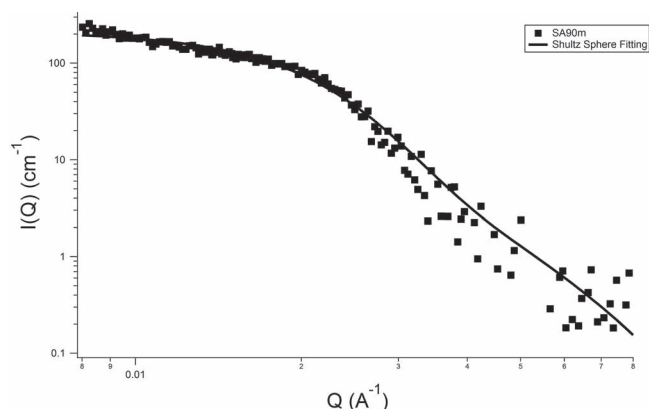
Figure 6. Fit of the structure factor of the as-cast and all solvent annealed samples to the scattering of a Shultz sphere, which models the pure PCBM phase. Parameters extracted from these fits are given in Table 4.

Table 4. Sphere (pure PCBM) radius, sphere (pure PCBM) vol%, solvent (P3HT rich phase) SLD, and PCBM (dispersed in P3HT rich phase) vol% in surrounding solvent (P3HT rich phase) for the sample with solvent annealing for 90 min (SA90m) determined from Shultz sphere model.

Sample	Radius (± 3 Å)	Pure PCBM (± 1%)	Solvent SLD (×10^{-6} A^{-2})	PCBM dispersed in P3HT rich phase (±1%)
SA90m	90	9%	1.68	27%

Table 5. Device performance at standard AM-1.5 illumination.

	AC	SA30m	SA60m	SA90m	TA
V_{OC} (V)	0.48	0.55	0.54	0.63	0.65
J_{SC} (mA/cm^2)	4.13	4.24	4.44	4.86	4.87
FF (%)	50	52	54	59	55
PCE (%)	1.0	1.2	1.3	1.8	1.7

P3HT:PCBM mixture while the SANS analysis provides information on the PCBM fraction in the amorphous P3HT, which should be higher than that from reflectivity experiments.

For the sample that has been solvent annealed for 90 min (SA90m), the scattering a low Q increases dramatically and the fit to an elliptical cylinder model indicates that the PCBM concentration reaches 55%, which is higher than the PCBM fraction in the whole sample. Therefore, this physically unrealistic result indicates that the elliptical cylinder model is not applicable for this sample. Hence the fitting of the SANS curves indicates that the as-cast, SA30m, and SA60m samples can be accurately modeled as P3HT crystals dispersed in an amorphous matrix that is a mixture of P3HT and PCBM, but the SA90m sample cannot.

The scattering curve of the sample that was solvent annealed for 90 min exhibits a scattering pattern that differs significantly from all other samples, does not fit the elliptical cylinder model, and thus is fit to a Schultz sphere model,[47] which describes a pure PCBM phase (spheres) that is dispersed in a P3HT rich phase (solvent). From the fitting, the PCBM domain radius, PCBM domain vol% in the whole sample, the P3HT rich phase SLD, and the vol% of PCBM in the P3HT rich phase are determined. Only the scattering from the SA90m sample reasonably fits to the Schultz sphere model, as presented in **Figure 6**. The structural parameters derived from this fit are presented in **Table 4**, which indicate that the radius of the PCBM phase is 90 Å and the volume fraction of the pure PCBM phase in the whole sample is ≈9%. This analysis shows that there remains PCBM dispersed in the P3HT phase at a level of 27%, which is consistent with its miscibility limit.

Hence, the solvent annealing of the bilayer that occurs from 60 to 90 min results in the phase separation of the PCBM from the P3HT domain, resulting in a formation of pure PCBM domains. The large contrast in SLD between the pure PCBM phase and the P3HT rich phase dominates the scattering, resulting in a dramatic increase in scattering. Moreover, the analysis of the scattering curve monitors the phase separation of the PCBM during SA, resulting in aggregates that are ≈90 Å, which compares favorably to the size of PCBM aggregates formed with thermal annealing (≈59 Å).[18]

2.4. Device Performance

The results reported above clearly document the evolution of structure that occurs in the solvent processed P3HT:PCBM bilayer with solvent annealing. In order for this information to be most useful, these structural changes must be correlated to OPV function. With this in mind, the photovoltaic properties of the P3HT:PCBM bilayer that are SA and TA were determined. These results are shown in **Table 5** and **Figure 7**. The open-circuit voltage (V_{OC}), short-circuit current (J_{SC}), fill factor (FF), and the power conversion efficiency (PCE) increases with SA time, where the PCE increases by 80% after SA for 90 min. The power conversion efficiency of these samples are noticeably lower than usually presented for P3HT:PCBM devices, which is a direct consequence of the fact that the active layer is significantly thinner (≈55 nm) than is optimal. To verify this, we have also tested the performance of thicker samples, which show power conversion efficiencies that are comparable to optimized devices. Moreover, these samples qualitatively mimic the improvement of device performance with solvent annealing that is observed for the thinner samples.
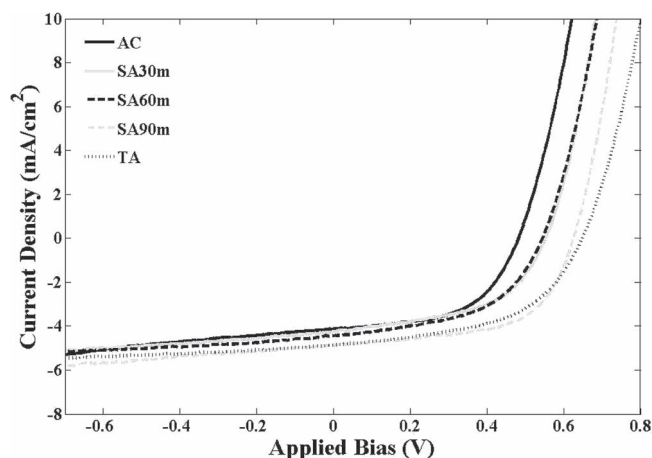
Figure 7. Current density vs. applied voltage curves.

The J_{SC} is associated with charge transport and dissociation of excitons and its variation with solvent annealing can be correlated to the observed structural changes. As shown in Table 5, J_{SC} slowly increases with SA for the first 60 min, which can be ascribed to the diffusion of PCBM into P3HT, resulting in an increase of donor/acceptor interfacial area and the number of excitons that are dissociated. The increase in crystallization of P3HT with solvent annealing facilitates hole transport, which also contributes to the increase of J_{SC}. Moreover, the dramatic increase of J_{sc} for the sample that is solvent annealed for 90 min can be directly ascribed to the formation of PCBM domains, which provide pathways for electrons to transport to the cathode and dramatically improve charge collection and power conversion efficiency.

3. Discussion

The controlled exposure of the solution processed P3HT:PCBM bilayer to *o*-dichlorobenzene (ODCB) vapor clearly alters the morphology and depth profile of the bilayer, which in turn impacts its ability to act as an active layer in an organic photovoltaic device. With solvent vapor annealing, the P3HT and PCBM molecules become more mobile, resulting in the simultaneous enhanced ordering of P3HT and diffusion of PCBM into P3HT, followed by the phase separation of PCBM.

During solvent vapor annealing, the P3HT matrix is swollen with the solvent. The increased molecular mobility allows the P3HT chains to crystallize, verified by the GIWAXS results. Moreover, the interdiffusion of PCBM and P3HT occurs simultaneously with the P3HT crystallization, which is verified by reflectometry. Meanwhile, at longer times the increase in P3HT crystallization appears to facilitate the phase separation of PCBM from P3HT. The increased mobility of P3HT and PCBM also gives freedom for the PCBM molecule to diffuse away from P3HT and PCBM evolves towards thermodynamically favorable larger agglomerates.

Contrasting the structural development with solvent annealing to that which occurs with thermal annealing provides additional insight into the role of crystallization and phase separation in the structural development in these complex mixtures. When 1:1 mixtures of P3HT and PCBM are annealed at 150 °C, P3HT quickly crystallizes and PCBM phase separates from the P3HT in a matter of seconds. Because of this rapid structural development, it is not clear whether the P3HT crystallization drives the phase separation or the crystallization and phase separation are independent processes.

Solvent vapor annealing however provides a more controlled process. The slow evaporation of a high boiling point solvent such as ODCB provides time for the solvent to plasticize the polymer and allow it to crystallize slowly. In this work, the evolution of the structure during solvent vapor annealing can be described as two stages: the first stage is the diffusion of PCBM into the P3HT, which occurs simultaneously with an increase in the crystallization of P3HT, processes that occur in the first 60 min. This is followed by a second stage that includes the phase separation of PCBM from the P3HT, agglomeration of PCBM and formation of pure PCBM phase. This last process occurs even though the extent of P3HT crystallinity does not

change during this latter solvent annealing process. It is therefore obvious that these results clearly indicate that the increase in P3HT crystallization does not, by itself, induce PCBM phase separation. During the first 60 min of solvent annealing, P3HT crystallinity increases at the same time that PCBM diffuses into the P3HT. The thermodynamic driving force of mixing drives the PCBM phase separation, as the PCBM miscibility limit is 22%.[45]

The change of morphology of the active layer in an OPV device dramatically impacts its photovoltaic performance, and therefore the correlation of structural development during solvent annealing to its OPV function is important. During the first 60 min of solvent annealing, the increased crystallinity of P3HT and diffusion of PCBM into the P3HT is mainly complete, however no significant change of J_{SC} and PCE is observed. Our interpretation of this result is that for early solvent annealing times, most PCBM are trapped in the amorphous P3HT phase, which limits the transport of electrons to the electrode, although the crystallization of P3HT facilitates hole transport. After solvent vapor annealing for 90 min, the pure PCBM phase forms, which facilitates electron transport. In our "rivers and streams" model,[32] the presence of the pure PCBM phase is required as a "river", to dramatically facilitate the charge transport to the electrode. Therefore, sufficient P3HT crystallization and the formation of a PCBM pure phase are crucial in the optimization of the morphology of the active layer.

In the current solvent annealing process, the exposure to solvent vapor provides a more controllable process than thermal annealing, which in turn offers a more detailed understanding of the structural development in OPV bulk heterojunctions. This process provides a unique method to control and optimize the morphology, depth profiles, and crystallinity of the conjugated polymer/fullerene mixture, and will be broadly applicable to a broad range of polymer/fullerene mixtures and advanced energy materials.

4. Conclusions

The structural development of a P3HT:PCBM solvent processed bilayer with controlled exposure to ortho-dichlorobenzene solvent vapor is examined. The results indicate that exposure of this solution-processed bilayer to ODCB solvent vapor alters the P3HT crystallinity and depth profiles very effectively, presumably by inducing mobility of the components as solvent plasticizes the mixture. Significant changes in the morphology of the bilayer films are observed during solvent vapor annealing. The interdiffusion of P3HT and PCBM and enhanced crystallization of P3HT occur simultaneously at the early stages of solvent annealing, followed by the phase separation of PCBM. Different from thermal annealing, where the structure develops in seconds, solvent vapor annealing provides an opportunity to develop a more detailed picture of the structural development in conjugated fullerene mixtures. In these bilayers, there are two stages in the structure development: interdiffusion of PCBM and P3HT and crystallization of P3HT in the first stage where the bilayer structure transitions to a bulk heterojunction structure; in the second stage, the phase separation of PCBM from P3HT and agglomeration of PCBM occurs, which provide

www.MaterialsViews.com

ADVANCED
FUNCTIONAL
MATERIALS
www.afm-journal.de

FULL PAPER

pathways for electrons to transport to the cathode during OPV function, dramatically improving charge transport, and resulting in a significant increase of short-circuit current and power conversion efficiency. Therefore, sufficient P3HT crystallization and formation of a PCBM pure phase are crucial in the optimization of the morphology of the active layer. Moreover, these results clearly document that the phase separation of PCBM from P3HT *is not* driven by P3HT crystallinity, but is due to the concentration of PCBM exceeding the miscibility limit of PCBM in P3HT.

5. Experimental Section

Materials: PCBM was purchased from Nano-C, and regioregular P3HT was purchased from Rieke Metals (Sepiolid P200, MW = 25 000 g/mol, PDI = 1.6, regioregularity, ≈98%). Both were used without further purification. To fabricate thin film bilayers, P3HT and PCBM was dissolved in ODCB (10 mg/mL) and dichloromethane (5 mg/mL), respectively, and filtered through 0.45 µm PTFE syringe filters. Prior to spin-coating, the silicon wafers were cleaned by immersion in a 3:1 (v/v) mixture of concentrated sulfuric acid and 30% (v/v) hydrogen peroxide, heated to ≈70 °C for 15 min, and rinsed with copious amounts of high purity water and dried under a stream of nitrogen. P3HT-PCBM bilayers were fabricated by first spin casting P3HT onto the clean silicon wafers at 1000 rpm for 60 s. The spin coated P3HT film (≈330 Å as determined by AFM and ellipsometry) was allowed to dry in an N_2 atmosphere for at least 30 min to remove residual solvent. A PCBM layer was then spin-coated onto the P3HT layer at 4000 rpm for 10 s. The fabricated bilayers remained in an unheated vacuum oven for 24 h to remove residual solvent. The thickness of the bilayer was about 550 Å, as measured by neutron reflectivity. Hence the volume fraction of PCBM in the "bilayer" was about 40%. The term bilayer is in quotes because the neutron reflectivity studies (Figure 3) and reports in the literature show that PCBM is distributed in the initial P3HT layer immediately after sample formation. Thus, the sample was indeed a bilayer, but each layer was initially a mixture of P3HT and PCBM.

Controlled solvent annealing of the bilayers was executed in an upright column. In this process, ODCB was added to the bottom of 100 cm long vertical column and allowed to equilibrate for 4 h, forming a constant vapor pressure gradient along the length of the column. In this column, the solvent vapor pressure was zero at the top of the column and the vapor pressure of the solvent at the solvent surface. The amount of solvent vapor that the P3HT:PCBM samples were exposed to was then controlled by the amount of time that the sample was in the column as well as the height at which it resided. The samples in this study were always left at a height that was 90% down the column. The thermal annealing was completed by heating the bilayer to 140 °C in a vacuum for 30 min (TA).

GIWAXS: X-ray diffraction from the thin films was completed with a high resolution ($\Delta 2\theta = 0.026°$) one-dimensional Phillips X'pert-Pro diffractometer in grazing-incidence geometry with a wavelength of 0.154 nm. The detector was a point-by-point krypton filled proportional counter and the samples were scanned in the z-direction, which meant that the results were reported as a function of q_z. The angle of incidence between the X-ray and the thin film surface was 0.3° for all samples.[48,49]

Neutron Reflectometry: All reflectivity measurements were completed on the Liquids Reflectometer at the Spallation Neutron Source at Oak Ridge National Laboratory with a neutron wavelength varying from 2.75–5.75 Å and an effective Q-range of 0.006–0.105 Å^{-1}. The calculated reflectivity of model scattering length density profiles were fit to the measured reflectivity curves of the samples using Layers[50] and Motofit Software[51] to determine the structure of the thin films.

The depth profiles of the spin-cast and subsequently annealed bilayers were modeled using 2–4 layers. In the fitting procedure, the scattering length density, thickness, and roughness of each layer were freely varied.

A model was assumed to accurately reflect the structure of the sample when the model reflectivity profile converges with the experimental profile, where the quality of fit was gauged using χ^2 statistics, and the mass balance of the model system was within 5% of the mass balance of the sample.

The SLD profile was then analyzed to obtain the concentration depth profile of each component in the system. For instance, the PCBM concentration depth profile was determined using Equation 2,

$$\phi(z)_{PCBM} = \frac{\rho(z) - \rho_{P_3HT}}{\rho_{PCBM} - \rho_{P_3HT}} \tag{2}$$

where $\varphi(z)_{PCBM}$ is the volume fraction of PCBM at depth z, $\rho(z)$ is the experimental scattering length density at depth z, and ρ_{P3HT} and ρ_{PCBM} are the SLD of P3HT and PCBM, respectively. In order to quantitatively analyze the reflectivity curves, the accurate scattering length density of each component is needed. The scattering length density of crystalline P3HT and amorphous P3HT were calculated to be 0.69 × 10^{-6} Å^{-2} ($\rho_{P3HT,c}$), and 0.62 × 10^{-6} Å^{-2} ($\rho_{P3HT,a}$), respectively,[46] while the SLD of amorphous PCBM was determined to be 4.4 × 10^{-6} Å^{-2} based on its density and composition, and measurements of the reflectivity of PCBM monolayers.[46]

SANS: SANS experiments were completed on the General Purpose SANS instrument at the High Flux Isotope Reactor at Oak Ridge National Laboratory. The raw data were corrected for scattering from the empty cell, detector dark current, and detector sensitivity. The corrected data were then normalized to an absolute scale using a Porasil-A standard. By evaluating the slope of IQ^4 versus Q^4 plots at high Q ($Q = 4\pi/\lambda \sin\theta$, where λ is the neutron wavelength and θ is the scattering angle), the contribution from incoherent scattering and thermal density fluctuations were eliminated, yielding the absolute coherent scattering.

Photovoltaic Device Fabrication and Characterization: Indium tin oxide (ITO) glass substrates were first washed with detergent and then cleaned in an ultrasonic bath using deionized (DI) water, acetone and isopropyl alcohol (IPA). The cleaned substrates were subsequently treated with UV ozone for 20 min. Filtered PEDOT:PSS (Baytron P 4083) was then spin cast on the UV-treated ITO glass at 4000 rpm for 40 s. After baking the PEDOT:PSS films in air at 140 °C for 20 min, the active layer was spin cast under the same conditions as above except for the concentration of P3HT in ODCB. Because of the different surface properties of silicon and PEDOT:PSS, a 7 mg/mL solution of P3HT in ODCB was prepared, rather than a 10 mg/mL solution, to obtain the same thickness of P3HT in all experiments. The active layer film thickness was about 55 nm. Solvent and thermal annealing of the active layer were carried out at the same conditions as described above. Finally, to create the OPV device, 40 nm of Ca and 60 nm of Al were thermally deposited on the film through a shadow mask. Current-voltage (I–V) characterization of the polymer photovoltaic cells was conducted using a Thermal Oriel 96000 300-W solar simulator under the lumination of AM1.5G, 100 mW/cm^2.

Supporting Information

Supporting Information is available from the Wiley Online Library or from the author.

Acknowledgements

[1] G. Yu, J. Gao, J. C. Hummelen, F. Wudl, A.J. Heeger, *Science* **1995**, *270*, 1789.

[2] J. Peet, J. Y. Kim, N. E. Coates, W. L. Ma, D. Moses, A. J. Heeger, G. C. Bazan, *Nat. Mater.* **2007**, *6*, 497.

[3] G. Li, V. Shrotriya, Y. Yao, J. S. Huang, Y. Yang, *J. Mater. Chem.* **2007**, *17*, 3126.

[4] G. Li, V. Shrotriya, J. S. Huang, Y. Yao, T. Moriarty, K. Emery, Y. Yang, *Nat. Mater.* **2005**, *4*, 864.

[5] L. M. Chen, Z. R. Hong, G. Li, Y. Yang, *Adv. Mater.* **2009**, *21*, 1434.

[6] S. Günes, H. Neugebauer, N. S. Sariciftci, *Chem. Rev.* **2007**, *107*, 1324.

[7] C. J. Brabec, N. S. Sariciftci, J. C. Hummelen, *Adv. Funct. Mater.* **2001**, *11*, 15.

[8] H.D. Zang, Y. Y. Liang, L. P. Yu, B. Hu, *Adv. Energy Mater.* **2011**, *1*, 923.

[9] H. Hoppe, N. S. Sariciftci, *J. Mater. Chem.* **2006**, *16*, 45.

[10] D. Motaung, G. Malgas, C. Arendse, C. Oliphant, D. Knoesen, *J. Mater. Sci.* **2009**, *44*, 3192.

[11] X. N. Yang, J. Loos, S. C. Veenstra, W. J. H. Verhees, M. M. Wienk, J. M. Kroon, M. A. J. Michels, R. A. J. Janssen, *Nano Lett.* **2005**, *5*, 579.

[12] H. J. Kim, H. H. Lee, J. J. Kim, *Macromol. Rapid Commun.* **2009**, *30*, 1269.

[13] Y. Zhao, Z. Y. Xie, Y. Qu, Y. H. Geng, L. X. Wang, *Appl. Phys. Lett.* **2007**, *90*, 043504.

[14] J. Jo, S. I. Na, S. S. Kim, T. W. Lee, Y. Chung, S. J. Kang, D. Vak, D. Y. Kim, *Adv. Funct. Mater.* **2009**, *19*, 2398.

[15] S. S. Van Bavel, E. Sourty, G. de With, J. Loos, *Nano Lett.* **2009**, *9*, 507.

[16] G. Li, Y. Yao, H. Yang, V. Shrotriya, G. Yang, Y. Yang, *Adv. Funct. Mater.* **2007**, *17*, 1636.

[17] S. Pal, S. Roy. A. K. Nandi, *J. Phys. Chem. B* **2005**, *109*, 18332.

[18] J. W. Kiel, A. P. R. Eberle, M. E. Mackay, *Phys. Rev. Lett.* **2010**, *105*, 168701.

[19] W. R. Wu, U. S. Jeng, C. J. Su, K. H. Wei, M. S. Su, M. Y. Chiu, C. Y. Chen, W. B. Su, C. H. Su, A. C. Su, *ACS Nano* **2011**, *5*, 6233.

[20] M. Kobashi, H. Takeuchi, *Macromolecules* **1998**, *31*, 7273.

[21] H. Sirringhaus, P. J. Brown, R. H. Friend, M. M. Nielsen, K. Bechgaard, B. M. W. Langeveld-Voss, A. J. H. Spiering, R. A. J. Janssen, E. W. Meijer, P. Herwig, D. M. de Leeuw, *Nature* **1999**, *401*, 685.

[22] Z. Bao, A. Dodabalapur, A. J. Lovinger, *Appl. Phys. Lett.* **1996**, *69*, 4108.

[23] H. Sirringhaus. H. Tessler, R. H. Friend, *Science* **1998**, *280*, 1741.

[24] R. J. Kline, M. D. McGehee, E. N. Kadnikova, J. Liu, J. M. J. Frechet, M. F. Toney, *Macromolecules* **2005**, *38*, 3312.

[25] C. W. Tang, *Appl. Phys. Lett.* **1986**, *48*, 183.

[26] J. S. Moon, C. J. Takacs, Y. Sun, A. J. Heeger, *Nano Lett.* **2011**, *11*, 1036.

[27] B. Watts, W. J. Belcher, L. Thomsen, H. Ade, P. C. Dastoor, *Macromolecules* **2009**, *42*, 8392.

[28] J. W. Kiel, B. J. Kirby, C. F. Majkrzak, B. B. Maranville, M. E. Mackay, *Soft Matter* **2010**, *6*, 641.

[29] N. D. Treat, M. A. Brady, G. Smith, M. F. Toney, E. J. Kramer, C. J. Hawker, M. L. Chabinyc, *Adv. Energy Mater.* **2011**, *1*, 82.

[30] D. Chen, F. Liu, C. Wang, A. Nakahara, T. P. Russell, *Nano Lett.* **2011**, *11*, 2071.

[31] K. H. Lee, P. E. Schwenn, A. R. G. Smith, H. Cavaye, P. E. Shaw, M. James, K. B. Krueger, I. R. Gentle, P. Meredith, P. L. Burn, *Adv. Mater.* **2011**, *23*, 766.

[32] W. Yin, M. Dadmun, *ACS Nano* **2011**, *5*, 4756.

[33] M. A. Ruderer, R. Meier, L. Porcar, R. Cubitt, P. Muller-Buschbaum, *J. Phys. Chem. Lett.* **2012**, *3*, 683.

[34] M. A. Ruderer, P. Muller-Buschbaum, *Soft Matter* **2011**, *7*, 5482.

[35] F. Liu, Y. Gu, J. W. Jung, W. H. Jo, T. P. Russell, *J. Polym. Sci. Polym. Phys.* **2012**, *50*, 1018.

[36] W. Chen, M. P. Nikiforov, S. B. Darling, *Energy Environ. Sci.* **2012**, *5*, 8045.

[37] M. A. Ruderer, S. Guo, R. Meier, H. Y. Chiang, V. Korstgens, J. Wiedersich, J. Perlich, S. V. Roth, P. Muller-Buschbaum, *Adv. Funct. Mater.* **2011**, *21*, 3382.

[38] B. A. Collins, J. R. Tumbleston, H. Ade, *J. Phys. Chem. Lett.* **2011**, *2*, 3135.

[39] S. Bertho, G. Janssen, T. J. Cleij, B. Conings, W. Moons, A. Gadisa, J. D'Haen, E. Goovaerts, L. Lutsen, J. Manca, D. Vanderzande, *Sol. Energy Mater. Sol. Cells* **2008**, *92*, 753–760.

[40] A. Swinnen, I. Haeldermans, M. vande Ven, J. D'Haen, G. Vanhoyland, S. Aresu, M. D'Olieslaeger, J. Mance, *Adv. Funct. Mater.* **2006**, *16*, 760.

[41] R. Hegde, N. Henry, B. Whittle, H. Zang, B. Hu, J. Chen, K. Xiao, M. Dadmun *Sol. Energy Mater. Sol. Cells* **2012**, *107*, 112.

[42] K. Balakrishnan, A. Datar, R. Oitker, H. Chen, J. M. Zou, L. Zang, *J. Am. Chem. Soc.* **2005**, *127*, 10496.

[43] K. C. Dickey, J. E. Anthony, Y. L. Loo, *Adv. Mater.* **2006**, *18*, 1721.

[44] L. Patterson, *Phys. Rev.* **1939**, *56*, 978.

[45] H. P. Chen, R. Hegde, J. Browning, M. D. Dadmun, *Phys. Chem. Chem. Phys.* **2012**, *14*, 5635.

[46] S. Kline, *J. Appl. Crystallogr.* **2006**, *39*, 895.

[47] G. V. Schulz, *Z. Phys. Chem.* **1939**, *B43*, 25.

[48] H. C. Yang, T. J. Shin, L. Yang, K. Cho, C. Y. Ryu, Z. N. Bao, *Adv. Funct. Mater.* **2005**, *4*, 671.

[49] H. Sirringhaus, P. J. Brown, R. H. Friend, M. M. Nielsen, K. Bechgaard, B. M. W. Langeveld-Voss, A. J. H. Spiering, R. A. J. Janssen, E. W. Meijer, P. Herwin, D. M. de Leeuw, *Nature* **1999**, *401*, 685.

[50] Layers is an Excel spreadsheet for modeling NR data developed by John Ankner at Oak Ridge National Laboratory.

[51] A. Nelson, *J. Appl. Cryst.* **2006**, *39*, 273.